Transillumination Imaging for Blood Oxygen Saturation Estimation of Skin Lesions

Brian D'Alessandro, Atam P. Dhawan, *Fellow, IEEE*

Abstract—Detecting the early stages of melanoma can be greatly assisted by an accurate estimate of subsurface blood volume and blood oxygen saturation, indicative of angiogenesis. Visualization of this blood volume present beneath a skin lesion can be achieved through transillumination of the skin. As the absorption of major chromophores in the skin is wavelength dependent, multispectral imaging can provide the needed information to separate out relative amounts of each chromophore. However, a critical challenge to this strategy is relating the pixel intensities observed in a given image to the wavelength dependent total absorption existing at each spatial location. Consequently, in this paper we develop an extension to Beer's law, estimated through a novel voxel-based, parallel processing Monte Carlo simulation of light propagation in skin which takes into account the specific geometry of our transillumination imaging apparatus. We then use this relation in a linear mixing model, solved using a multispectral image set, for chromophore separation and oxygen saturation estimation of an absorbing object located at a given depth within the medium. Validation is performed through Monte Carlo simulation, as well as by imaging on a skin phantom. Results show that subsurface oxygen saturation can be reasonably estimated with good implications for the reconstruction of 3D skin lesion volumes using transillumination towards early detection of malignancy.

Index Terms—transillumination, multispectral imaging, melanoma, skin lesions, skin cancer

I. INTRODUCTION

SKIN cancer is the most common form of malignancy, but the survival rate is very high if the cancer is detected, diagnosed, and treated early. To assist in this early detection, a hand held imaging device known as the Nevoscope [1] utilizes the principles of optical imaging and transillumination to better observe the subsurface structure of a skin lesion, such as the depth of the lesion and the blood volume surrounding the lesion. This device directs light into the skin at a 45 degree angle through a fiber optic ring placed directly against the skin surface. Light diffuses through the skin tissue, and photons which scatter back through the lesion up to the surface are captured by a charge-coupled device (CCD) image sensor attached to the Nevoscope (see Fig. 1). Since surface illumination is also blocked, the geometry of this illumination device essentially creates a virtual light source behind the skin lesion, thus providing a transilluminated image which contains important subsurface features for the early detection of skin cancer. By filtering the light source, a multispectral image set of the lesion can also be obtained, providing additional information which can be exploited for analysis [2].

Brian D'Alessandro (email: bmd5@njit.edu) and Atam P. Dhawan (email: dhawan@njit.edu) are with the Department of Electrical and Computer Engineering, New Jersey Institute of Technology, Newark, NJ 07102 USA.
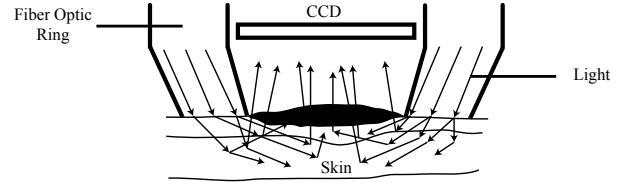
Fig. 1. Nevoscope Geometry

One challenge associated with this method of imaging skin lesions is accurately measuring the concentration of subsurface skin features from the 2D images. The pixel intensity seen in a certain pixel location in an image depends on the concentration, mixture, and depth of the main subsurface chromophores in skin. Concentration mixture is represented by the overall absorption coefficient, from which the concentration of individual chromophores can be separated by multispectral imaging [3]. The absorption of main chromophores in the skin (oxyhemoglobin (HbO_2), deoxyhemoglobin (Hb), and melanin) varies depending on wavelength (see Fig. 2). Thus, by comparing the localized absorption difference between two or more wavelengths, it is possible to obtain a measure of how much spectral distortion is caused by blood and melanin absorption. Of course, because of the diffusive nature of light in tissue, the actual absorption coefficient at specific locations within the volume is difficult to obtain. A precise quantitative result is further confounded by scattering and the photon path of Nevoscope illumination.

Hence, as a step toward estimating the spatially dependent total absorption for multispectral chromophore separation, in this paper we present an extension to Beer's law for light transmission through an object in a medium, which is tailored to the geometry of the Nevoscope device and is valid for objects located at a given depth within the medium (a preliminary version of which has appeared in [4]). The extension is developed by use of a novel voxel-based, parallel processing Monte Carlo simulation of light propagation from the Nevoscope ring through the skin. First, we discuss the development and improvements related to our simulation. Then, we use the adjusted Beer's law equation, along with the multispectral imaging set and a linear mixing model, to estimate the relative concentration of oxyhemoglobin and deoxyhemoglobin in an object embedded in the skin, first using simulated images and later using real images with the Nevoscope and a skin phantom.

II. MONTE CARLO SIMULATION

Monte Carlo simulation is a statistical technique for simulating random processes, and has been applied to light-tissue
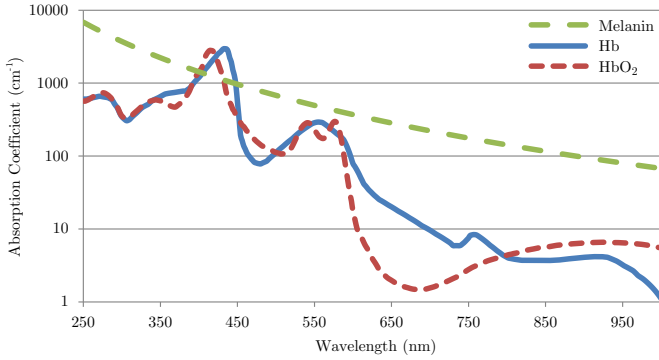
Fig. 2.   Absorption spectra of Melanin, Hb, and HbO$_2$ [5], [6].

interactions under a wide variety of situations [7]–[12]. The basic idea of a Monte Carlo simulation for light transport in tissue is to mathematically propagate one photon at a time through a virtual environment. This photon is subjected to absorption and scattering events, which depend on the optical properties of the photon's location, tissue boundary interactions, and also a measure of randomness. When a large number of these photons are simulated, the stochastic nature of each individual photon's path averages out to a good approximation of light transport and diffusion through the entire tissue. For further information about Monte Carlo simulation for light transport in tissue, the reader is directed to [13], [14].

The most commonly simulated tissue models used in Monte Carlo simulations assume tissues to be layered structures with homogeneous properties within each layer [9], [10]. Although these models are simple and easy to implement, real tissues are geometrically more complex and consist of non-homogeneous layers. Instead, a voxel-based approach [11] represents an object as a set of discrete volume elements known as voxels, analogous to pixels in a 2D image. The accuracy with which irregular boundaries can be described using the voxel-based approach depends on the number and resolution of the voxels. This approach has been successfully used to simulate skin tissue transillumination by the Nevoscope [15].

While there are many advantages to Monte Carlo simulation, one drawback is that it is computationally expensive. Since the method simulates the path of each photon individually, the time for computation is directly proportional to the number of photons simulated. Furthermore, since the method is stochastic in nature, a large number of photons is always desired as this increases the signal-to-noise ratio and accuracy of the resulting simulated images. A number of techniques have been implemented to speed up the Monte Carlo simulation and reduce redundant computation [16], including running a Monte Carlo simulation once in absorption-less tissue and then applying the absorption effects afterward to approximate the results on a volume with absorption, or by detecting backscattered light in one slice of a ring, and then rotating the results to all other angular slices [15], [17]. However, such modifications can be cumbersome, more difficult to deal with post-simulation, and even less accurate. Fortunately, the speed of processing has increased as time has passed, and lately, the huge benefit of parallel processing has mitigated the need for anything but a straightforward implementation of the Monte Carlo simulation in tissue.

In this work, a graphics processing unit (GPU) with NVIDIA's Compute Unified Device Architecture (CUDA) is used for the Monte Carlo simulation of photon transport within tissue. This problem lends itself very well to massively parallel computation as it requires millions or even billions of simulated photons, each of which run through the same general steps and are independent of each other. Essentially, each photon is represented by a single thread on the GPU. Thus, instead of simulating one photon after another on a serial CPU, hundreds of threads can be created on the GPU, thereby simulating hundreds of photons at the same time. The number of simulated photons can thus be easily scaled into the tens and hundreds of millions of photons, or even billions.

The MCML (Monte Carlo for Multi-Layered media) program is one example of serial photon simulation [9]. This popular program has been used extensively to model light transport in multilayered tissue by a number of researchers over the years. More recently, an implementation of MCML was released, known as CUDAMCML, which makes use of the CUDA environment on a GPU to speed up the MCML algorithm nearly 1000 times [18]. This speed improvement is certainly noteworthy, since a simulation which might take over a day to simulate with MCML might only take a few minutes or less with CUDAMCML. The CUDAMCML program is no different in functionality than MCML, both simulate a multilayered tissue with results given in polar coordinates by cylindrical volumes and pie shaped detectors.

In this work, the CUDAMCML program has been modified to provide additional functionality while still retaining the speed improvement inherent from using the GPU for processing. The first improvement made is to use a square grid detector rather than a pie shaped detector. This pixel-based orientation likens itself more readily to comparison with a camera CCD and is easier to visualize. Similarly, the energy distribution volume of the tissue is obtained through a voxel grid with XYZ coordinates rather than a cylindrical polar grid in RAZ coordinates. Another notable difference in the presented implementation is that the tissue is constructed with a voxel-based geometry where each voxel may be assigned a different set of optical properties, rather than a layered geometry with homogenous layers as done in MCML and CUDAMCML. A voxel-based model allows for a much wider variety of possible tissue models and representations of complex objects embedded in the tissue. Furthermore, the specific Nevoscope geometry was defined within the simulation for use along with the parallel architecture. The improvements made to CUDAMCML provide greater flexibility in modeling and simulating the Nevoscope while still retaining the GPU-based speed improvements compared to the original MCML program.

A. Parallel Nevoscope Monte Carlo Simulation

The life of a single simulated photon begins at its launch. The most straightforward way to simulate the photon launch

is through a single point light source infinitely narrow in dimension. This essentially results in the impulse response of the system. However, in reality a light source always has some specific dimension, and thus for a more accurate simulation, the area of this source beam must be taken into account. To do so, some have used the convolution method for symmetric tissue volumes, which assumes the system to be linear and invariant [16]. The response of the system to the point source is convolved over the actual area of the light source to produce the final result. This reduces the number of photons needed for simulation. However, convolution cannot be used for irregular volumes, and with the ability for parallel computing on a graphics card, the number of photons is less of a limitation. As a result, the simplest method of simulating a light source of a given area or shape is to simply randomly distribute the initial location of each photon equally over the necessary area. Thus, to simulate the Nevoscope light source evenly distributed within a ring with inner radius r_1 and outer radius r_2, independent uniform random numbers ξ_1 and ξ_2 on the open interval $(0,1)$ are generated to find the initial random x and y coordinates of a photon:

$$
\begin{aligned}
x &= \sqrt{\left(r_2^2 - r_1^2\right)\xi_1 + r_1^2}\cos\left(2\pi\xi_2\right) \\
y &= \sqrt{\left(r_2^2 - r_1^2\right)\xi_1 + r_1^2}\sin\left(2\pi\xi_2\right) \quad (1)
\end{aligned}
$$

The Nevoscope is a ring light source with a ring thickness of 1 mm. Additionally, the optical fibers within the Nevoscope head are oriented at a $45°$ polar angle downwards towards the center of the ring, and so the direction vector of a new photon must be adjusted accordingly depending on its initial azimuthal angle used in (1) with respect to the ring center, by:

$$
\begin{aligned}
dx &= -\sqrt{2}/2 \cdot \cos\left(2\pi\xi_2\right) \\
dy &= -\sqrt{2}/2 \cdot \sin\left(2\pi\xi_2\right) \quad (2) \\
dz &= \sqrt{2}/2
\end{aligned}
$$

where dx, dy, and dz are the x, y, and z components of the photon direction vector, respectively. The direction vector is normalized such that $\sqrt{dx^2 + dy^2 + dz^2} = 1$.

As previously mentioned, implementation of this Monte Carlo simulation was done using the NVIDIA CUDA software development kit which defines the interface to execute code on an NVIDIA graphics card. Support for a multi-GPU setup was also implemented, using an NVIDIA GeForce GTX 560 Ti and 9800 GT, for a speedup of over 20%. Upon initialization of the Monte Carlo code, the total number of photons desired to be simulated was divided between the two graphics cards: 77.5% was assigned to the GTX 560 Ti, while 22.5% was assigned to the 9800 GT. The difference balances out the speed differences between the two cards, and allows both GPUs to finish simulation at approximately the same time, thus maximizing the efficiency. In this way, over one billion photons can be simulated in 102 seconds, demonstrating a speedup of over $3000\times$ compared to our previous implementation executing serially on a conventional processor.

III. Linear Mixing Model

Given such an improvement in speed with the voxel-based parallel processing Monte Carlo simulation, it was desired to use this simulation to develop and test a methodology for the unmixing of chromophore concentrations and distributions in skin. To describe the effects of chromophore distribution on backscattered light, diffusion theory has often been used as an approximation of the radiative transport equations to model light propagation in tissue [7], [19]. Solutions to the diffusion equation generally show an exponential attenuation of light in a medium for a given depth, with the wavelength dependent absorption and scattering coefficients as $\mu_a(\lambda)$ and $\mu_s(\lambda)$. To simplify, a minimum penetration depth level is assumed among all selected wavelengths for ratiometric chromophore analysis, and μ_s is assumed to be constant over the selected spectral bandwidth. Considering these constraints, for a specific wavelength λ, the total amount of absorption seen at the skin surface, or, the diffused light remittance intensity $\mu_a(\lambda)$ at a particular pixel, is related to the absorption of each chromophore present in the medium at that particular pixel. Although the spatial dependence of the absorption coefficients cannot be *exactly* known because of the depth-dependent diffuse nature of light propagation and heterogeneity of skin tissue, these absorptions are assumed to be linearly combined for imaging. Since the major chromophores in the skin are melanin, HbO$_2$, and Hb, the total absorption is a function of the unknown amount of melanin [Mel], oxyhemoglobin [HbO$_2$], and deoxyhemoglobin [Hb]:

$$
\mu_a(\lambda) = [\text{Mel}]\mu_a^{\text{Mel}}(\lambda) + [\text{HbO}_2]\mu_a^{\text{HbO}_2}(\lambda) + [\text{Hb}]\mu_a^{\text{Hb}}(\lambda) \quad (3)
$$

where $\mu_a^{\text{Mel}}(\lambda)$, $\mu_a^{\text{HbO}_2}(\lambda)$, and $\mu_a^{\text{Hb}}(\lambda)$ are the wavelength dependent absorption coefficients of melanin, HbO$_2$, and Hb. With three unknowns, three equations, or three images taken at different wavelengths, are needed to estimate the amounts of each chromophore. Given the absorption coefficients of melanin, HbO$_2$, and Hb, the linear system defined by the three equations can be used to estimate [Mel], [HbO$_2$], and [Hb] present under the area imaged by the pixel.

The [HbO$_2$] estimate itself relates to how much spectral absorption is caused by HbO$_2$, and therefore, is a measure of blood oxygen content. Another method of visualization is to compute a ratiometric measurement defining the blood oxygen saturation, [SO$_2$], relative to the total amount of blood. Total blood is simply [HbO$_2$]+[Hb], therefore the normalized ratiometric measurement of percent oxygen saturation in the blood is:

$$
[\text{SO}_2] = \frac{[\text{HbO}_2]}{[\text{HbO}_2] + [\text{Hb}]} \quad (4)
$$

The aforementioned equations are evaluated pixel-by-pixel, resulting in 2D solutions for [Mel], [HbO$_2$], [Hb], and [SO$_2$]. Hence, the linear assumption is made on a pixel-by-pixel basis, which allows for inhomogeneously distributed chromophores in the x-y plane. Inhomogeneity can still be present along the z-axis, however at present we assume a homogenous mixture which is visible from images of the skin surface.

IV. Pixel Intensity to Absorption Coefficient Relation

In the linear mixing model of (3), the overall absorption $\mu_a(\lambda)$ at a particular pixel in the transilluminated images is

assumed to be a linear combination of the amounts of each chromophore modified by the absorption coefficient of that chromophore. However, the question remains as to how the overall absorption is related to the observed pixel intensity in the image. This problem is a case of light transmission through an absorbing chromophore object, so an initial approximation can be made using the Beer–Lambert law, although for illumination using the Nevoscope geometry, this approximation will need to be improved.

A. Beer's Law

As light propagates through a turbid medium such as the skin, the intensity of light decreases due to absorption and scattering interactions with the medium. The extent of these interactions are characterized by the absorption and scattering coefficients, μ_a and μ_s. At the simplest level, μ_a is related to a change in light intensity by the Beer–Lambert law (or Beer's law for short), which states that for light transmitted through a medium over a path length of ℓ,

$$I/I_0 = e^{-\mu_a \ell} \qquad (5)$$

where the incident light intensity is I_0, and the transmitted light intensity is I.

Because Beer's law only takes into account attenuated effects of absorption, not scattering, many attempts have been made to introduce and quantify the scattering corrections needed for Beer's law [20]–[23]. Such corrections can be mathematically complex, through reliance on solutions to the radiative transfer equation or other modeling. Others only account for scattering effects on straight laser-like transmission, but do not propose solutions for light which is back-scattered [22], [23]. For highly scattering media, such as biological tissue, the diffusion equation is often used as an approximation of the radiative transport equation, where the dominant term in its solution for a semi-infinite slab is approximated by [24]–[26]:

$$\Phi(\ell) \sim C \cdot e^{-\mu_{\text{eff}} \ell} \qquad (6)$$

where $\Phi(\ell)$ is the fluence rate, C is a constant and

$$\mu_{\text{eff}} \approx \sqrt{3\mu_a[\mu_a + (1-g)\mu_s]} \quad \text{if } \mu_a \ll \mu_s \qquad (7)$$

Consequently, an approximate scattering-corrected equation to Beer's Law may be written as:

$$I/I_0 = e^{-\mu_{\text{eff}} \ell} \qquad (8)$$

In the Nevoscope geometry for skin lesion imaging, the angled fiber optic ring emits light directly into the skin tissue which allows the back-scattered light alone to be imaged. Therefore, in (5) and (8), the light intensity I is the intensity value which is directly read by a CCD detector, and can thus be likened to the image pixel value at each pixel location. Similarly, the incident light intensity I_0 may be represented by the intensity of the same pixel in an image of skin background, or, the transilluminated light without any lesion absorption interference. In practice, a background image would be acquired on the patient on a nearby patch of skin, right next to the lesion. By normalizing with respect to this background,
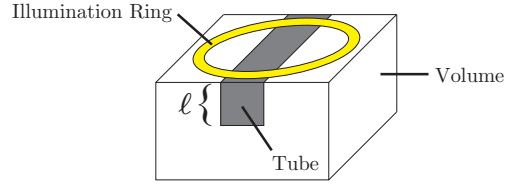

Fig. 3. Rectangular tube of depth ℓ embedded in a voxel grid volume.

melanin absorption due to the patient's skin color is effectively canceled out which eliminates this potential variable from analysis. Thus in the normalized image defined by I/I_0, any additional melanin or blood due to the lesion itself will be visible as dark regions ($I/I_0 < 1$), whereas the skin surrounding the lesion will have I/I_0 approximately equal to 1. In this simplified model, ℓ represents the depth of a homogenous absorbing object adjacent to the skin surface. Furthermore, since the model is a pixelated image-based representation, the relevant equation variables I, I_0, μ_a, and ℓ are all functions of pixel location (x, y), and can therefore vary heterogeneously in the x-y plane.

The "true" relationship between the background corrected image I/I_0 and μ_a is defined as an unknown function f:

$$I/I_0 = f(\ell, \mu_a) \qquad (9)$$

The shape of this function can be observed through simulation using the previously described voxel-based Monte Carlo simulation of light propagation [27], [28]. To measure this true relationship of I/I_0 versus μ_a for an object embedded in skin, a small "tube" with a rectangular cross-section was defined within a $24 \times 24 \times 100$ virtual voxel grid, representing a physical size of $1.2 \times 1.2 \times 0.5$ cm^3. The embedded tube, with a width of 1 mm and a varying depth of ℓ, was defined in the uppermost layers of the volume (see Fig. 3).

The surface detector was defined to be a 7×7 grid, with each pixel of size 0.7 mm^2. The absorption coefficient of this tube was then set to increasing values, spanning $\mu_a = 0$ cm^{-1} to 50 cm^{-1}. For each value of μ_a in the tube, the simulation produced an image I, from which the average intensity value was computed over pixels within the tube region of interest. Multiple simulations were also run for varying depths of the tube, spanning $\ell = 0.25$ mm to 2 mm. The resulting scatter plots of I/I_0 versus μ_a are visualized as circles in the graphs of Fig.s 4 and 5. Only plots for tube depths of 0.25 mm and 0.5 mm are shown in the figure.

These simulated data points are compared to the predicted values produced by (5) in Fig. 4, as well as (8) in Fig. 5. In each plot, the solid line represents the predicted curve while the plotted circles represent measurements from the Monte Carlo simulation.

B. Beer's Law with Nevoscope Geometry Adjustment

As is evident from Fig.s 4 and 5, there exists a clear discrepancy between simulated observation and mathematical approximation. Use of the scattering correction provided by (8) improves the match compared to (5) alone. Furthermore, (8) matches better for small depths, but the discrepancy between
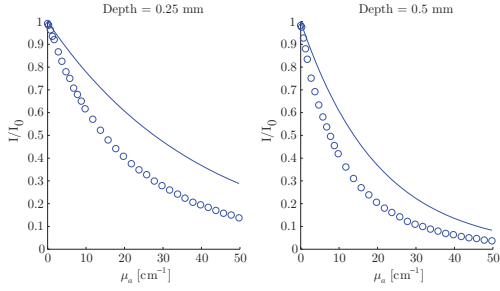
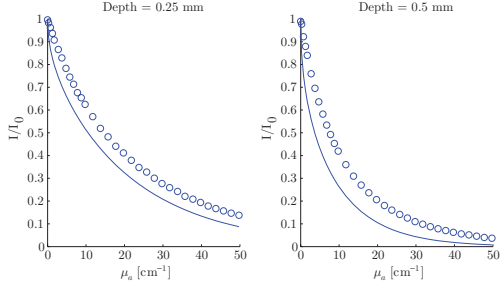Fig. 4. True I/I_0 vs. μ_a (circles), compared with (5) (solid lines).

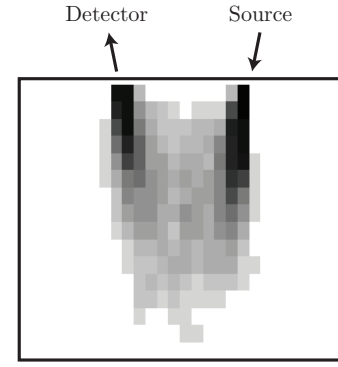Fig. 5. True I/I_0 vs. μ_a (circles), compared with (8) (solid lines).

Fig. 6. Example source-detector average photon path through a tissue volume with a point light source.
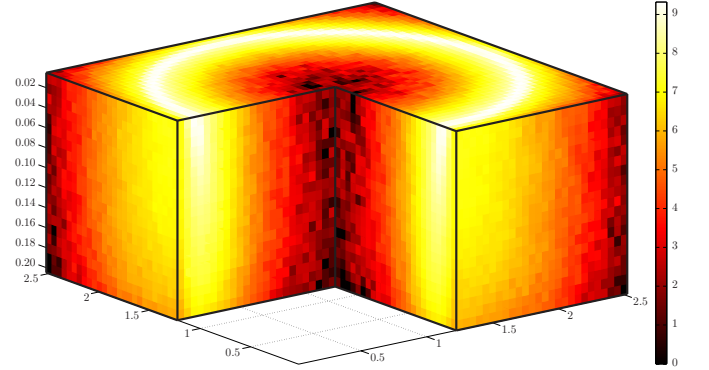

Fig. 7. Photon positions within a simulated tissue using 10^6 photons. The color scale represents the log of the number of photons passing through each displayed voxel. Volume dimensions are in cm.

the approximated equation and reality increases as the object extends deeper.

It is not surprising that these discrepancies exist, because the geometry of illumination using the Nevoscope is not straight transmission, as Beer's law is designed for. Rather, the actual path of Nevoscope light is U-shaped, originating from the fiber optic ring, passing down through the skin and the lesion, and finally traveling back up to the surface. That the light takes this specific shape on average can be proven through Monte Carlo simulation. Fig. 6 shows the average photon path between a single source and single detector through a Monte Carlo simulated tissue volume. Note the U-shaped profile characteristic of diffuse reflectance with the Nevoscope geometry. To further visualize Nevoscope light distribution in the tissue, Fig. 7 shows the number of photons which pass through each voxel in the volume, after illumination by the Nevoscope ring. Light intensity is highest near the ring, but drops off at further distances according to the absorption and scattering events.

Thus, to compensate for this geometric characteristic a correction factor R is introduced to (8) such that:

$$f(\ell, \mu_a) \sim e^{-\mu_{\text{eff}}\ell} \cdot e^{-\ell R} \qquad (10)$$

Simulation and surface fitting was performed to estimate this μ_a- and depth-dependent correction factor R. The effect of μ_s differences in the wavelength range used was found to not have a significant effect on pixel intensity ($< 2\%$ difference over the range of depth and μ_a values), so a fixed value was assumed within μ_{eff}. The correction factor which provided an optimal fit between the observed data and corrected equation is given by:

$$R = -\left(4.5(\mu_a)^{0.18}\ell^{0.031} + 6.2\mu_a\ell\right) \qquad (11)$$

Thus, the final complete corrected equation is given by:

$$\begin{aligned}I/I_0 &= \exp\left(-\ell\sqrt{3\mu_a[\mu_a + 13.86]}\right) \\ &\quad \cdot \exp\left(4.5(\mu_a)^{0.18}\ell^{1.031} + 6.2\mu_a\ell^2\right)\end{aligned} \qquad (12)$$

Comparison between the observed simulated data points and this new corrected equation are visualized in Fig. 8. Naturally, the equation plot is designed to fit the data well, and this is the case over a large range of object depths ℓ.

C. Additional Correction for Objects Below the Surface

The aforementioned equations work well for an object which borders the surface of the simulated skin, but what about the case where an object is present deep within the tissue
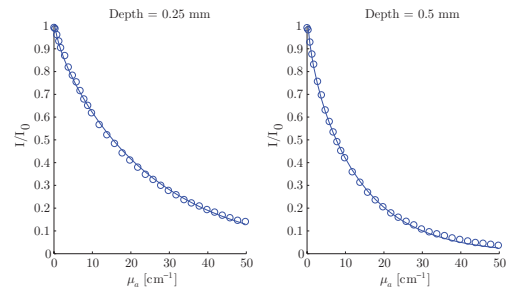

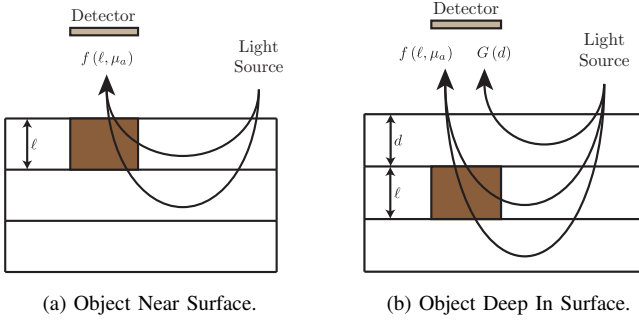Fig. 8. True I/I_0 vs. μ_a (circles), compared with (12) (solid lines).

Fig. 9. Difference in detected light for objects at varying depths within the volume.

volume? In this case, the light detected at the surface, I/I_0, will have an additional component of light which does not pass through the object, but rather scatters through the upper layers of the volume (see Fig. 9). This component $G(d)$ depends on the distance d between the object and the surface and represents the fraction of light which is detected despite the presence of the object. $G(d)$ was approximated by simulating deep embedded objects where the absorption of the object was so high that no light was able to pass through. It was found that:

$$I/I_0 = G(d) + (1 - G(d)) f(\ell, \mu_a) \qquad (13)$$

where

$$G(d) = -9.25d^2 + 5.92d - 0.0294 \qquad (14)$$

V. CHROMOPHORE SEPARATION

Given the correction factor which allows for an extended Beer's law equation specific to the Nevoscope illumination geometry, it is desired to utilize (12) for the estimation of the unknown relative amounts of chromophores in the skin. In this situation, μ_a must first be estimated at each pixel location given I/I_0 and an estimate of ℓ. Hence, a spatially dependent image map of μ_a is found by inverting (9), where f is approximated by (12) to find:

$$\mu_a = f^{-1}(\ell, I/I_0) \qquad (15)$$

Solutions to this equation are evaluated for each pixel within each image obtained in the multispectral imaging set to find $\mu_a(\lambda)$, the absorption image map at wavelength λ. Subsequently, multiple linear regression can be performed pixel-by-pixel using the linear mixing model of (3) to find [Mel], [HbO$_2$], and [Hb].

The linear mixing model presented here assumes that while chromophore concentrations can vary heterogeneously in the x-y plane, embedded objects are homogenous in the z dimension. Accurately recovering an irregular mixture of chromophores with respect to depth is a much more difficult and ill-posed problem. However, with this reliable function for relating $\mu_a(\lambda)$, ℓ, and the image pixel intensity values in I/I_0, the function can be used as *a priori* knowledge for an inverse reconstruction algorithm to recover a best estimate of the 3D structure of the imaged skin lesion [28], [29]. Based on our parallel work in this area, we have found that this prior

TABLE I
MONTE CARLO SIMULATION PARAMETERS

	680 nm	780 nm
$\mu_a^{\text{HbO}_2}$ [cm^{-1}]	1.49	3.80
μ_a^{Hb} [cm^{-1}]	12.90	5.76
μ_s [cm^{-1}]	112.87	94.83
g	0.846	

knowledge is able to assist the reconstruction procedure for a faster and more accurate estimation of the melanin and blood volumes of a skin lesion, towards early detection of malignant lesions.

VI. RESULTS

A. Monte Carlo Simulation

To test the ability of (12) to assist in the estimation of chromophore amounts in the skin, a simulation was devised whereby the same virtual volume and tube setup as described previously was used. In this case, the depth of the tube was set to ℓ=1 mm, and the absorption coefficient of the tube was set such that the tube contained a mixture of HbO$_2$ and Hb. Multispectral imaging simulations were performed at 680 nm and 780 nm (see Table I for a list of parameters used in simulation), and the system of equations for the linear mixing model was solved for the unknown amounts [HbO$_2$] and [Hb], with lesion [Mel] assumed to be zero. Baseline skin absorption was set as $0.244 + 85.3 \exp(-(\lambda - 154)/66.2)$ cm^{-1} [6]. The unmixing procedure was performed using each of the three discussed methods of relating detector intensity to absorption coefficient for comparison. The results are shown in Fig. 10, relating the estimated [SO$_2$] fraction to the true [SO$_2$] fraction. In each plot, the solid line represents the ideal case where the estimated fraction equals the true fraction.

While unmixing using (5) in Fig. 10(a), or (8) in Fig. 10(b) show large errors especially towards situations with low oxygen saturation, the corrected method using (12) in Fig. 10(c) produces unmixing which is nearly linear, demonstrating accurate estimation of the unknown [SO$_2$] fraction in a simulated environment for the entire range of possible [SO$_2$] values.

Furthermore, using the updated (13) to allow for objects between 1-2 mm and 2-3 mm below the surface of the skin, chromophores can still be separated with good accuracy, although the accuracy degrades for the deeper object due to increased noise as a result of less light penetration (see Fig. 11). As the dermis, which contains the blood vessels beneath the skin, only extends down around 3 mm [30], depths beyond this limit are less practical for Nevoscope imaging.

B. Skin Phantom

While chromophore separation was successful using Monte Carlo simulation, it was also desired to test the method in the real world using the actual Nevoscope. To do so, the Nevoscope was used to image a skin phantom [31] containing an embedded circular capillary tube of inside diameter 1.15 mm, whose center was situated 0.575 mm below the surface.
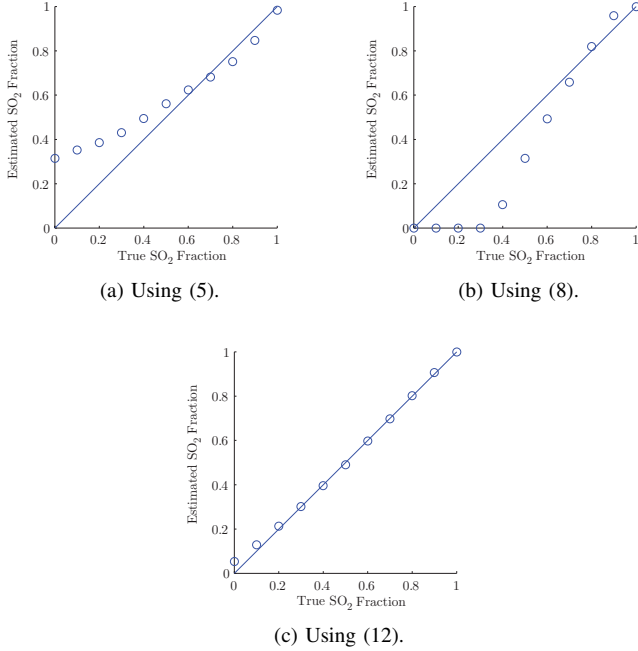
(a) Using (5).

(b) Using (8).

(c) Using (12).

Fig. 10. Chromophore separation of Monte Carlo simulated [HbO$_2$] and [Hb] using the various equations for ℓ=1 mm.

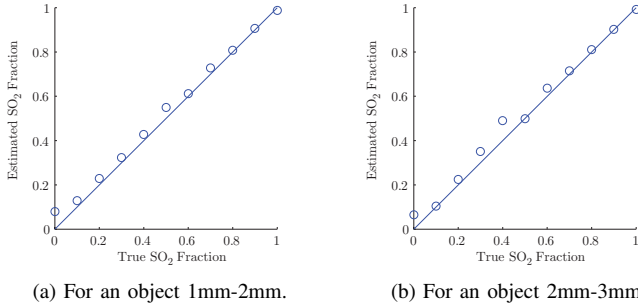

(a) For an object 1mm-2mm.

(b) For an object 2mm-3mm.

Fig. 11. Chromophore separation for a Monte Carlo simulated deep object.

The capillary tube was filled with varying fractions of artificial HbO$_2$ and Hb (red and blue food coloring). The optical absorption coefficients of these artificial substitutes were measured experimentally using a single integrating sphere. Based on the measured μ_a, two wavelengths were selected for transillumination imaging: 600 nm was chosen for being a near-isosbestic point, while 875 nm was chosen for providing the largest μ_a ratio between the two chromophores. Similarly for real HbO$_2$ and Hb, 600 or 800 nm could be used as an isosbestic point, while 680 nm could be used as a second separating wavelength. Equation (12) was used with $\ell = 0.903$ mm, representing the average depth of the circular tube.

The plot of the estimated [SO$_2$] fraction versus the true [SO$_2$] fraction is presented in Fig. 12 with corresponding numerical values detailed in Table II. The resulting image estimates of [HbO$_2$] and [Hb] are presented in Fig. 13. It is clear that the relative oxygen saturation ratio can be reasonably estimated from multispectral imaging and (12), even for real world imaging using the actual imaging apparatus and a skin

TABLE II
SKIN PHANTOM CHROMOPHORE SEPARATION

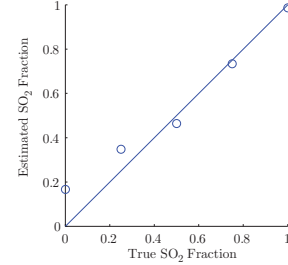| True [HbO$_2$]	True [Hb]	Estimated [HbO$_2$]	Estimated [Hb]
100%	0%	98.68%	1.32%
75%	25%	73.36%	26.64%
50%	50%	46.40%	53.60%
25%	75%	34.85%	65.15%
0%	100%	16.60%	83.40%

Fig. 12. Skin phantom chromophore separation graph.

phantom. The accuracy is best for high levels of [SO$_2$], while the accuracy decreases somewhat as [SO$_2$] is reduced to zero. However, as [SO$_2$] in human blood is usually around 75%, the better accuracy is seen in the most important range. The unmixing results prove the applicability of the adjusted equation outside of simulation.

VII. CONCLUSION

The successful demonstration of chromophore quantification shows that it is feasible to find a reasonable estimation of two chromophores in the skin based on multispectral images using the Nevoscope. Estimation of the relative concentrations of oxygenated blood and deoxygenated blood is critical to the detection of angiogenesis. Furthermore, the extended Beer's Law equation could provide a method of generating a pixel-by-pixel initial guess for an iterative inverse lesion volume reconstruction algorithm for early detection of skin cancers.

REFERENCES

[1] A. P. Dhawan, "Apparatus and method for skin lesion examination," U.S. Patent 5,146,923, September 15, 1992.
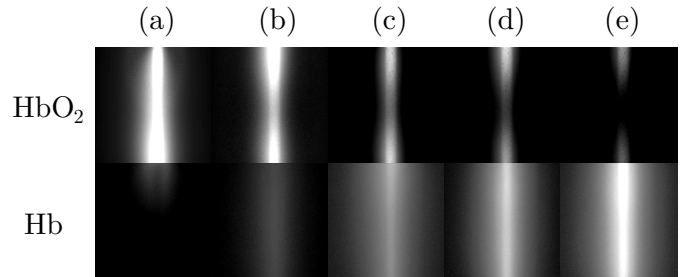

Fig. 13. Skin phantom chromophore separation images for (a) 100% HbO$_2$ & 0% Hb; (b) 75% HbO$_2$ & 25% Hb; (c) 50% HbO$_2$ & 50% Hb; (d) 25% HbO$_2$ & 75% Hb; (e) 0% HbO$_2$ & 100% Hb

[2] B. D'Alessandro, A. P. Dhawan, and N. Mullani, "Computer aided analysis of epi-illumination and transillumination images of skin lesions for diagnosis of skin cancers," in *Proceedings of the 33rd Annual International Conference of the IEEE Engineering in Medicine and Biology Society (EMBC '11)*, Boston, MA, August 30 - September 3, 2011, pp. 3435–3438.

[3] B. D'Alessandro and A. P. Dhawan, "Depth-dependent hemoglobin analysis from multispectral transillumination images," *IEEE Transactions on Biomedical Engineering*, vol. 57, no. 10, pp. 2568–2571, 2010.

[4] ——, "Blood oxygen saturation estimation in transilluminated images of skin lesions," in *Biomedical and Health Informatics (BHI), 2012 IEEE-EMBS International Conference on*, Hong Kong, Shenzhen, China, January 5-7 2012, pp. 729–732.

[5] S. Prahl. (1999, December 15) Optical absorption of hemoglobin. Oregon Medical Laser Center. [Online]. Available: http://omlc.ogi.edu/spectra/hemoglobin/

[6] S. L. Jacques, "Skin optics," *Oregon Medical Laser Center News*, January 1998. [Online]. Available: http://omlc.ogi.edu/news/jan98/skinoptics.html

[7] J. M. Schmitt, G. X. Zhou, E. C. Walker, and R. T. Wall, "Multilayer model of photon diffusion in skin," *Journal of the Optical Society of America. A, Optics and image science*, vol. 7, no. 11, pp. 2141–2153, 1990.

[8] S. T. Flock, M. S. Patterson, B. C. Wilson, and D. R. Wyman, "Monte carlo modeling of light propagation in highly scattering tissues - i: Model predictions and comparison with diffusion theory," *IEEE Transactions on Biomedical Engineering*, vol. 36, no. 12, pp. 1162–1168, 1989.

[9] L. Wang, S. L. Jacques, and L. Zheng, "MCML - monte carlo modeling of light transport in multi-layered tissues," *Computer Methods and Programs in Biomedicine*, vol. 47, no. 2, pp. 131–146, 1995.

[10] C. M. Gardner and A. J. Welch, "Monte carlo simulation of light transport in tissue: unscattered absorption events," *Applied Optics*, vol. 33, no. 13, pp. 2743–2745, 1994.

[11] I. G. Zubal and C. R. Harrell, "Voxel based monte carlo calculations of nuclear medicine images and applied variance reduction techniques," *Image and Vision Computing*, vol. 10, no. 6, pp. 342–348, 1992.

[12] M. Keijzer, S. L. Jacques, S. A. Prahl, and A. J. Welch, "Light distributions in artery tissue: Monte carlo simulations for finite-diameter laser beams," *Lasers in Surgery and Medicine*, vol. 9, no. 2, pp. 148–154, 1989.

[13] L. V. Wang and H.-i. Wu, *Biomedical Optics: Principles and Imaging*. Hoboken, NJ: John Wiley & Sons, Inc., 2007.

[14] V. Tuchin, *Tissue optics: light scattering methods and instruments for medical diagnosis*. SPIE-International Society for Optical Engineering, 2007.

[15] S. V. Patwardhan, A. P. Dhawan, and P. A. Relue, "Monte carlo simulation of light-tissue interaction: Three-dimensional simulation for trans-illumination-based imaging of skin lesions," *IEEE Transactions on Biomedical Engineering*, vol. 52, no. 7, pp. 1227–1236, 2005.

[16] L. Wang, S. L. Jacques, and L. Zheng, "CONV - convolution for responses to a finite diameter photon beam incident on multi-layered tissues," *Computer Methods and Programs in Biomedicine*, vol. 54, no. 3, pp. 141–150, 1997.

[17] S. Wang and A. P. Dhawan, "Shape-based multi-spectral optical image reconstruction through genetic algorithm based optimization," *Computerized Medical Imaging and Graphics*, vol. 32, no. 6, pp. 429–441, 2008.

[18] E. Alerstam, T. Svensson, and S. Andersson-Engels, "Parallel computing with graphics processing units for high-speed monte carlo simulation of photon migration," *Journal of biomedical optics*, vol. 13, no. 6, p. 060504, 2008.

[19] S. Chandrasekhar, *Radiative Transfer*. New York: Dover Publications, Inc, 1960.

[20] W. G. Tam and A. Zardecki, "Multiple scattering corrections to the beer-lambert law. 1: Open detector," *Applied Optics*, vol. 21, no. 13, pp. 2405–2412, Jul 1982.

[21] L. Wind and W. W. Szymanski, "Quantification of scattering corrections to the beer-lambert law for transmittance measurements in turbid media," *Measurement Science and Technology*, vol. 13, no. 3, pp. 270–275, 2002.

[22] E. Berrocal, D. Sedarsky, M. Paciaroni, I. Meglinski, and M. Linne, "Laser light scattering in turbid media part i: Experimental and simulated results for the spatial intensity distribution," *Optics Express*, vol. 15, no. 17, pp. 10 649–10 665, 2007.

[23] ——, "Laser light scattering in turbid media part ii: Spatial and temporal analysis of individual scattering orders via monte carlo simulation," *Optics express*, vol. 17, no. 16, pp. 13 792–13 809, 2009.

[24] W. Cheong, S. Prahl, and A. Welch, "A review of the optical properties of biological tissues," *IEEE Journal of Quantum Electronics*, vol. 26, no. 12, pp. 2166–2185, dec 1990.

[25] A. Ishimaru, *Wave Propagation and Scattering in Random Media*. New York: IEEE Press, 1999.

[26] S. A. Prahl, "Light transport in tissue," Ph.D. dissertation, The University of Texas at Austin, December 1988.

[27] L. Wang and S. L. Jacques, *Monte Carlo Modeling of Light Transport in Multi-layered Tissues in Standard C*. University of Texas, M.D. Anderson Cancer Centre, 1992.

[28] B. D'Alessandro and A. P. Dhawan, "Voxel-based, parallel simulation of light in skin tissue for the reconstruction of subsurface skin lesion volumes," in *Proceedings of the 33rd Annual International Conference of the IEEE Engineering in Medicine and Biology Society (EMBC '11)*, Boston, MA, August 30 - September 3, 2011, pp. 8448–8451.

[29] ——, "3d volume reconstruction of skin lesions for melanin and blood volume estimation and lesion severity analysis," *IEEE Transactions on Medical Imaging*, to be published.

[30] R. R. Anderson and J. A. Parrish, "The optics of human skin," *Journal of Investigative Dermatology*, vol. 77, no. 1, pp. 13–19, 1981.

[31] M. Lualdi, A. Colombo, B. Farina, S. Tomatis, and R. Marchesini, "A phantom with tissue-like optical properties in the visible and near infrared for use in photomedicine," *Lasers in Surgery and Medicine*, vol. 28, no. 3, pp. 237–243, 2001.

Brian D'Alessandro received the B.S. (summa cum laude), M.S., and Ph.D. degrees in computer engineering all from the New Jersey Institute of Technology (NJIT), Newark, New Jersey, in 2008, 2009, and 2012 respectively.

Presently, he is working as an Image Analysis Scientist with Canfield Scientific, Fairfield, New Jersey, developing algorithms for skin feature detection. He has previous intern and research experience with IBM and the University of Medicine and Dentistry of New Jersey. His research interests include image processing, medical imaging, computer vision, digital signal processing, pattern classification, and audio quality detection.

Dr. D'Alessandro was twice selected as a Student Paper Competition Finalist in the International Conference of the IEEE EMBS, in both 2010 and 2011.

Atam P. Dhawan (F'08) obtained his bachelor's and master's degrees from the Indian Institute of Technology, Roorkee, and Ph.D. from the University of Manitoba, all in Electrical Engineering. Currently he is a Distinguished Professor of Electrical & Computer Engineering and Interim Dean of Albert Dorman Honors College at NJIT, and Adjunct Professor of Radiology at the University of Medicine and Dentistry of New Jersey.

Dr. Dhawan has published more than 210 research articles in refereed journals, books, and conference proceedings. His current research interests are medical imaging, multimodality medical image analysis, adaptive learning and pattern recognition. His research work has been funded by NIH, NSF and several industries. Dr. Dhawan is a recipient of Martin Epstein Award (1984), National Institutes of Health FIRST Award (1988), Sigma-Xi Young Investigator Award (1992), University of Cincinnati Faculty Achievement Award (1994) and the prestigious IEEE Engineering in Medicine and Biology Early Career Achievement Award (1995) and University of Toledo Doermann Distinguished Lecture Award (1999). Dr. Dhawan has chaired numerous NIH special emphasis and review panels including the NIH Chartered Study Section on Biomedical Computing and Health Informatics (2008-11). He is Senior Editor of IEEE Transactions of Biomedical Engineering and Editor-In-Charge of IEEE TBME Letters. He is also Co-Editor-In-Chief of the new open-access IEEE Journal of Translational Engineering in Health and Medicine. He was the Conference Chair of the IEEE 28th International Conference of Engineering in Medicine and Biology Society, New York in 2006. He is the Conference Chair of IEEE International Conference on Point-of-Care Healthcare Technologies to be held in Bangalore India, January 16-18, 2013.